Spatter oxidation during laser powder bed fusion of Alloy 718: Dependence on oxygen content in the process atmosphere
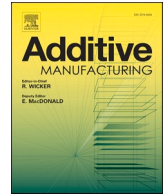
N.B. When citing this work, cite the original published paper.

(article starts on next page)

Contents lists available at ScienceDirect

Additive Manufacturing

Research Paper

Spatter oxidation during laser powder bed fusion of Alloy 718: Dependence on oxygen content in the process atmosphere

Ahmad Raza [a],[*], C. Pauzon [a], E. Hryha [a], Andreas Markström [b], P. Forêt [c]

[a] *Chalmers University of Technology, Department of Industrial and Materials Science, Gothenburg, Sweden*
[b] *Thermo-Calc Software AB, Stockholm, Sweden*
[c] *Linde AG, Unterschleissheim, Germany*

ARTICLE INFO

ABSTRACT

In laser powder bed fusion (L-PBF), powder degradation is mainly driven by the accumulation of highly oxidized spatter particles in the powder bed. Although the amount of spattering can be controlled by the melt pool stability, spatter formation is an unavoidable characteristic of PBF processes. Oxidized spatter risks defect formation in the printed components. However, the factors influencing the level of spatter oxidation during L-PBF processing are not yet fully understood. Herein, the residual oxygen in the process atmosphere was reduced from the traditionally applied 1000–20 ppm using an oxygen partial pressure control system to process Alloy 718 powder. Spatter particles accumulated on the gas inlet were further analyzed to reveal the effect of the oxygen content in the process atmosphere on the spatter oxidation by scanning electron microscopy (SEM) and X-ray photoelectron spectroscopy (XPS). Increasing the residual oxygen in the process atmosphere increased surface coverage by oxide phases rich in Al and Cr. The XPS analysis confirmed that the surface of Alloy 718 spatter particles were covered with Al- and Cr-based oxides, whose thickness increased with the oxygen content in the process atmosphere. The bulk oxygen content in the spatter powder showed the same trend with approximately thrice the oxygen content in spatters generated at 1000 ppm O_2 (608 ppm O in the sample) compared to spatters generated with oxygen at 20 ppm (206 ppm O in the sample). Thermodynamic simulations demonstrate a transition from thick Al- and Cr-based mixed corundum and spinel-type oxides to Al-based corundum oxide with decreasing oxygen partial pressure, consistent with the XPS findings.

1. Introduction

A paradigm shift is expected in the manufacturing industry due to the potential advancement granted by additive manufacturing (AM), as it allows the production of complex designs with limited material waste. Given the possible application of AM in the aerospace industry and energy sector, process development for superalloys is vital [1]. The superalloy Alloy 718 is widely produced by powder bed fusion (PBF) techniques, using electron beams or lasers as energy sources. Alloy 718 is a Ni-Fe-based superalloy whose strength is achieved after homogenization using a two-step aging treatment: firstly, a disc-shaped $\gamma''(\text{Ni}_3\text{Nb})$ phase is precipitated to enhance the strength at elevated temperatures; an additional $\text{Ni}_3(\text{Al, Ti})$ cuboid γ' phase is then precipitated, further contributing to the precipitation strengthening [2].

Powder degradation during PBF has been evidenced for various alloy systems, during electron beam powder bed fusion (EB-PBF) because of

the long-term exposure to high temperatures ($> 1000\ °C$), despite the vacuum [1,3], and during L-PBF with the formation of oxidized spatters [4–8]. During the processing of Alloy 718 by PBF techniques, the exposure of the powder characterized by high specific surface areas ($\sim 0.1\ \text{m}^2/\text{g}$) [3] to the high temperatures and residual oxygen in the process chamber results in oxidation of the critical alloying elements such as Al and Ti [6,9], which can affect the precipitation hardening [1]. Additionally, the oxidation can lead to the incorporation of oxide inclusions and related defects in the built material and negatively affect the properties of the final product [10]. The extent of powder oxidation depends on the susceptibility of the constituents to oxidation, exposure time, and conditions, such as the temperature and composition of the processing atmosphere [9]. Alloys containing elements with high oxygen affinity, such as Al, Ti, and Cr, among others, can show rapid initial oxidation of powder particles to form a protective oxide layer on the powder surface, which hinders further oxidation [7,11]. However,
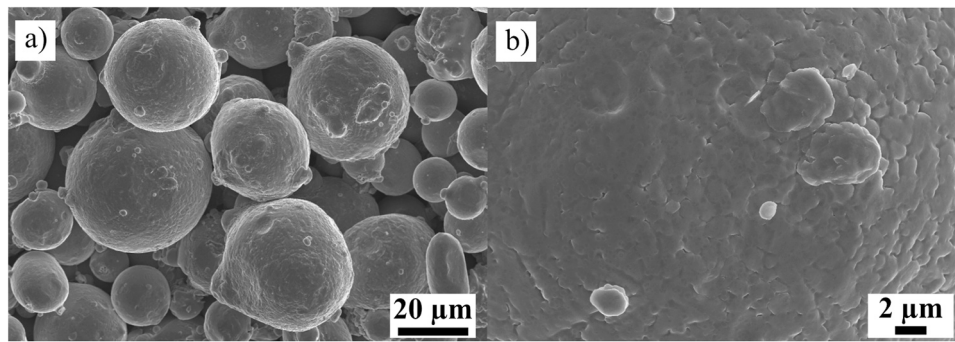
Fig. 1. SEM micrograph of the virgin gas atomized Alloy 718 powder used as feedstock in this study at × 2000 (a) and × 10,000 (b) magnification.

repeated exposure to the AM environment can enhance critical powder oxidation, as confirmed by Gruber et al. [1]. Their systematic study on Alloy 718 powder recycled over 30 cycles in EB-PBF showed an increase in Al_2O_3 particulate formation on the powder surface proportional to the number of cycles. With L-PBF, typically completed under 1000 ppm O_2, Cr and Al diffusion to the Alloy 718 powder particle surfaces and subsequent formation of oxide particulates and patches rich in these elements is expected [8].

In L-PBF, spatter accumulation in the powder feedstock is the main reason for the powder degradation [7]. According to a study by Gasper et al. [4] on Hastelloy X, 30–60% of spatter particles are incorporated in reused powder due to their similar particle size compared to the remainder of the powder bed. Hence, the oxidation of spatter particles can introduce a significant number of oxide defects in the fabricated parts. Various factors affect the spatter generation during L-PBF, including the volumetric energy density (VED), the type of alloy, the process gas and its purity, and the chamber environment [6,10,12–14]. Gunenthiram et al. [15] compared Al12Si and 316L stainless steel alloys; the Al12Si showed significantly reduced spatter generation due to droplet incorporation in the melt pool without ejection of spatters, in contrast to 316L stainless steel processing [15]. Their work also showed that a higher VED resulted in a higher number of spatters because of the melt pool instability. In another study, Pauzon et al. [16] demonstrated that the process gas type affects spatter generation, with He reducing the amount of spatters compared to the traditional Ar.

Our recent work [8] highlighted that Alloy 718 spatter particles, redepositing at different positions in the L-PBF process chamber, accumulated a significant amount of oxygen from the environment. For example, it was confirmed that spatters collected on the gas inlet and outlet exhibited significant surface coverage by oxide features. The oxygen content in spatters largely surpassed that of the virgin powder (by approximately 600 ppm). It was also established that characterization of the spatters at the gas inlet and outlet enabled tracking of the increase in the powder bed degradation, as these typically redeposit on the process area. This indicates a potential to reduce the oxidation of spatter particles by reducing the partial pressure of oxygen in the L-PBF chamber using atmosphere purity control systems as presented elsewhere [6,17, 18].

In the present study, a systematic approach was adopted to understand the spatter oxidation mechanism and dominating oxidizing elements in relation to the residual oxygen content in the L-PBF chamber atmosphere. For this purpose, the oxygen partial pressure in the process chamber was reduced from the commonly used 1000–20 ppm O_2, and spatter samples were collected from the gas inlet at 1000, 800, 600, 400, and 20 ppm oxygen partial pressure. A comprehensive X-ray photoelectron spectroscopy (XPS) analysis of spatter particles was conducted to understand the variation in the nature and amount of oxides. Detailed thermodynamic and kinetic simulations were performed using the software Thermo-Calc to associate the findings from XPS data with the fundamentals of metallurgy. These calculations helped link the

Table 1
Chemical range for the Alloy 718 feedstock powder in wt% specified by the manufacturer and the composition used for the Thermo-Calc calculations.

Element	wt%	Thermo-Calc (wt %)	Element	wt%	Thermo-Calc (wt %)
Ni	53.95	54	Co	0.01	
Cr	18.28	18.3	Mn	0.02	0.02
Fe	Balance	18.18	B	0.001	
Nb	5.12	5	Si	0.03	
Mo	3.04	3	Cu	0.04	
Ti	1.02	1	N	90	
Al	0.5	0.5	O	150	
C	0.05		P	< 0.01	
Ta	< 0.01		S	< 0.005	

oxidation and diffusion of certain elements to the available residual oxygen content. The analysis was further complemented by high-resolution scanning electron microscopy and bulk chemical analysis.

2. Materials and methods

Gas atomized Alloy 718 powder characterized by particles ranging from 15 to 45 μm in size with spherical morphology, supplied by EOS GmbH, was used in this study; see Fig. 1. Its composition is presented in Table 1. The composition was measured by the manufacturer using a range of techniques. For example, inductively coupled plasma (ICP) technique was used for metals except for lead, bismuth, and selenium, where AA/graphite was used. A combustion test was used for carbon and sulfur. Moreover, oxygen, nitrogen, and hydrogen were measured by fusion. The sample fabrication was conducted on an EOS M290 (EOS GmbH) L-PBF machine, equipped with a 400 W nominal power Yb-fiber laser and a build envelope of 250 × 250 × 325 mm³. Samples were produced using standard process parameters provided by the machine manufacturer with a layer thickness of 40 μm (under the license *IN718_PerformanceM291 2.11*). High-purity technical Ar (*Argon 5.0* with maximum 2 ppm oxygen) was used as the process gas. An external oxygen monitoring system was connected to the L-PBF machine: the ADDvance®O2 precision (Linde GmbH). During the operation of the ADDvance®O2 precision (Linde GmbH) system, the holding gas flow for the machine, typically present to limit leaks, was manually shut off to stabilize the residual oxygen level. This system enables control of the residual oxygen in the chamber by adjusting the high-purity gas flow within the recirculation system. It measures and controls the purity using an electrochemical cell. The system was used in the present work to repeat the same printing cycle under a controlled oxygen content in the build chamber, with an accuracy of 10 ppm measured with an electrochemical cell, to a minimal level of 20 ppm as well as 400, 600, 800, and 1000 ppm of residual O_2.

During L-PBF processing, a typical deposit on the gas inlet in the build chamber is formed by spatters traveling against the gas flow (toward the gas inlet). These deposits were carefully collected for analysis
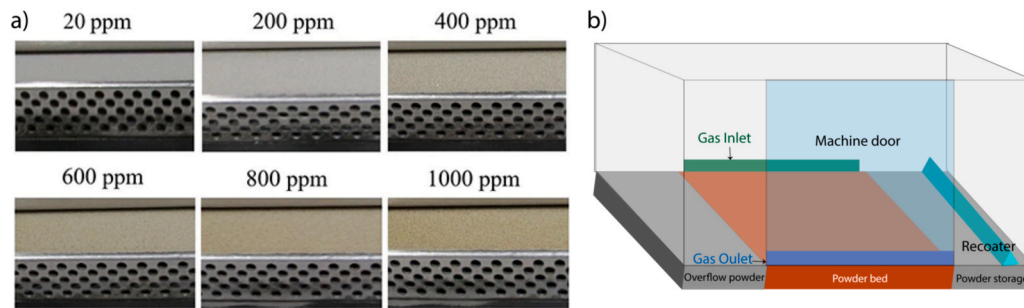
Fig. 2. (a) Alloy 718 powder deposited on the gas inlet and (b) a schematic of the interior of the EOS M290 machine highlighting the gas inlet and outlet positions. The discoloration of the deposited spatters is apparent and related to the higher amount of residual oxygen in the process atmosphere.

Table 2

Oxygen and nitrogen contents in the Alloy 718 virgin powder and the spatters collected under the studied oxygen levels in the L-PBF processing atmosphere.

Sample	Oxygen content [ppm]	Nitrogen content [ppm]
Virgin powder	150	90
Spatter 20 ppm O_2	206	107
Spatter 400 ppm O_2	390	118
Spatter 600 ppm O_2	479	125
Spatter 800 ppm O_2	592	123
Spatter 1000 ppm O_2	608	117

after each printing cycle, with different oxygen levels in the investigated processing gas. These deposits were characterized by distinctive discoloration (Fig. 2), associated with the residual oxygen in the process atmosphere. As the gas inlet position varies in different LB-PBF systems, Fig. 2b shows a schematic to illustrate the position of the gas inlet with respect to the powder bed in the EOS 290 machine.

The bulk oxygen content of the powder samples collected on the gas inlet was measured by a combustion technique using a LECO ON836 instrument. The surface morphology and microstructure of the collected samples were studied by high-resolution scanning electron microscopy (HR-SEM) using a LEO Gemini 1550 SEM microscope equipped with an INCA X-sight detector for energy dispersive X-ray spectrometry (EDS).

The effect of the oxygen partial pressure on the surface chemistry of spatter particles in terms of surface chemical composition, thickness, and distribution of chemical compounds on the powder surface as a function of etch depth was investigated by XPS using a PHI 5500 system (ULVAC-PHI). The PHI 5500 system was equipped with a mono-chromator Al Kα source (1486.6 eV). The powder particles were mounted on a pure indium plate by light pressing to avoid damage to the powder surface during sample preparation. For depth profile analysis, an Ar^+ ion gun was used. The etch depth was calibrated against a standard Ta_2O_5 sample; thus, the etch depth is given in Ta_2O_5 units. The data obtained from XPS were analyzed using PHI MultiPak software. The surface coverage by different oxide species was analyzed based on the oxide cation concentrations calculated from the narrow energy scans over the binding energies for the elements of interest, and further relative concentrations of Ti, Cr, and Al oxide cations were compared. The XPS analysis was performed based on a methodology developed for XPS analysis of powder, presented in detail elsewhere [19,20].

Thermodynamic calculations were performed using Thermo-Calc 2021a with the TCNI10 (Ni-Alloys v10.0) and TCOX10 (Metal Oxide Solutions v10.1) databases to investigate variations in the equilibrium phase fraction with increasing oxygen pressure. Additionally, the MOBNI5 (Ni-Alloys Mobility v5.1) database was employed for diffusion calculations using the diffusion module DICTRA in Thermo-Calc.

3. Results and discussion

Table 2 lists the oxygen contents measured by combustion analysis

for the different powder samples. The results highlight a significant increase in oxygen content from the virgin powder to the spatter (of at least 50 ppm, ~ 30%) and a consistent oxygen gain with increasing residual oxygen in the process atmosphere, leading to an increase of up to 450 ppm of oxygen or a fourfold increase compared with the original powder feedstock. Additionally, the nitrogen content analysis showed an increase of approximately 20 ppm (~ 20%) from the spatter compared to the virgin powder.

Fig. 3 displays micrographs of the studied spatter samples for selected residual oxygen levels. The collected particles appear to be mainly entrained particles from the powder bed since they have similar morphology to the feedstock powder, including some irregular particles that can also be observed in the virgin powder, as shown elsewhere [8]. The term "entrained particles" refers to the particles ejected by gas or vapor-induced entrainment during laser scanning of the powder bed. This is consistent with observations of the L-PBF process by Ly et al. [12], which showed that spatters originating from the melt pool are fewer than the entrained particles. The high-magnification micrographs highlight gradual surface degradation of the particles collected on the gas inlet with higher residual oxygen levels in the process atmosphere. Even for the highest purity atmosphere, signs of changes in the surface morphology and chemical composition are identified in the particles compared to the virgin powder (Fig. 1), with the formation of bright finely dispersed oxide particulates (Fig. 3). The surface coverage by the oxide also features a size increase corresponding to the residual O_2 in the process atmosphere. This is indicated by brighter or darker contrast, indicating potential differences in their composition and structure.

A qualitative chemical analysis by EDS of the areas highlighted in Fig. 4 is presented in Table 3 for a virgin powder particle and a spatter produced under 1000 ppm of residual O_2. This indicates that brighter and darker oxide features observed on the spatter surfaces are enriched with Al and Cr compared with the as-received surface. It also shows a higher oxygen signal compared with the surrounding powder surface. Finally, it is noteworthy that the degradation of the powder particles is localized on one side of the particles rather than uniformly distributed over the particle surface, indicating local oxidation due to local over-heating of the spatter particle, as also shown elsewhere [3].

Fig. 5 compares the XPS survey scans of the virgin powder surface in the as-received state and after 4 nm etching with those of particles collected on the inlet under varying residual oxygen levels (< 20 to 1000 ppm). The peaks from nickel, oxygen (O1s), and carbon (C1s) were distinguished along with the peaks of the alloying elements Cr, Ti, Al, Nb, and Fe. Interestingly, no nitrogen peak was observed, highlighting the rather inert behavior of Alloy 718 powder in relation to the residual N_2 molecules in the atmosphere remaining from purging the build chamber. This is also consistent with the nitrogen content in the powder; see Table 2. A Na1s peak appeared at ~ 1070 eV with an Auger peak for $NaKL_{23}L_{23}$ at 495 eV. Trace amounts of Na impurities were probably already present in the powder from the fabrication process and enriched the surfaces of the spatter particles at higher residual oxygen levels.

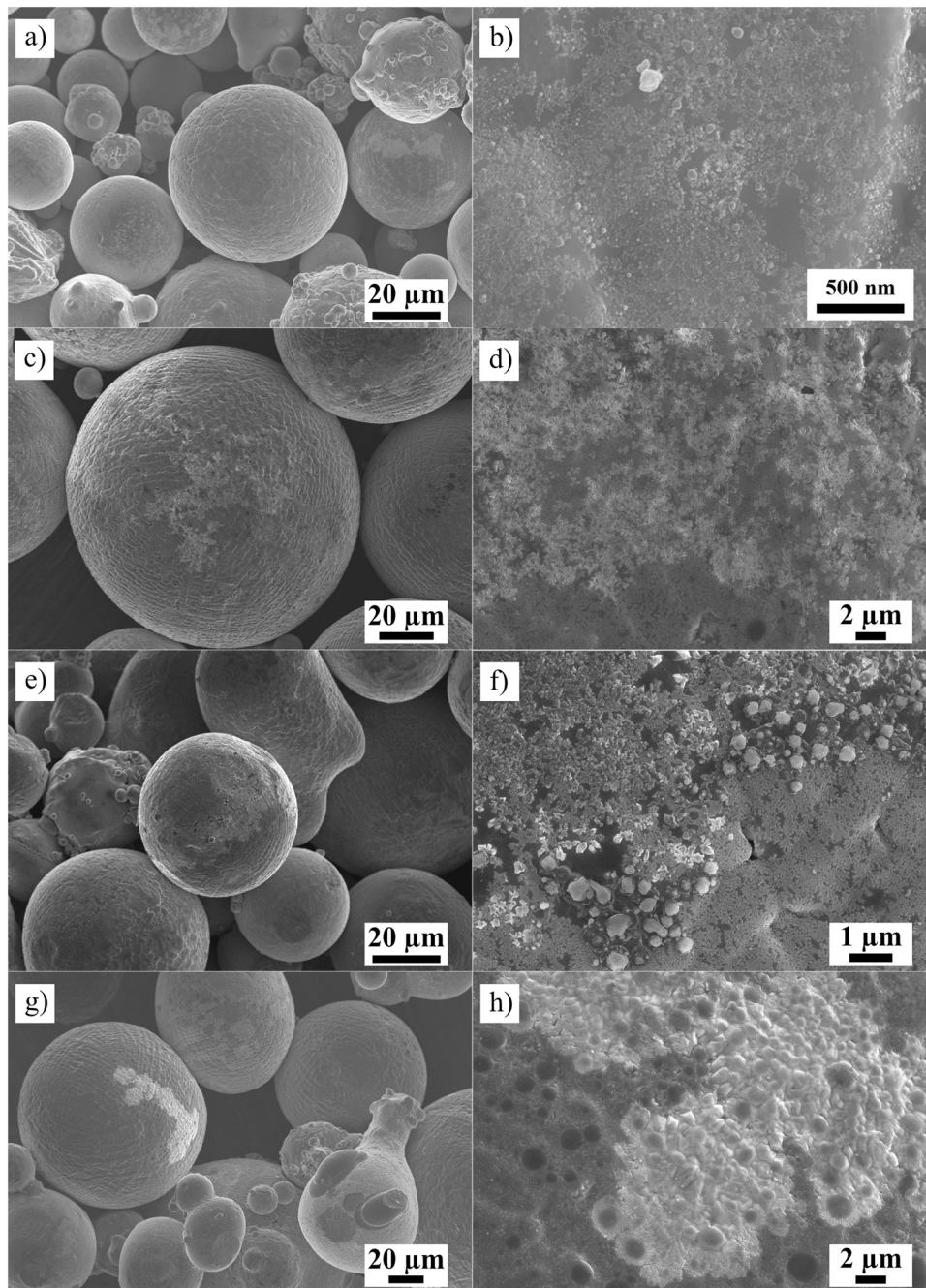The most significant differences between the powders were observed

Fig. 3. SEM micrographs of the Alloy 718 powder particles collected on the gas inlet after L-PBF processing at residual oxygen levels in process atmospheres of (a and b) 20 ppm, (c and d) 400 ppm, (e and f) 600 ppm, and (g and h) 1000 ppm O_2.
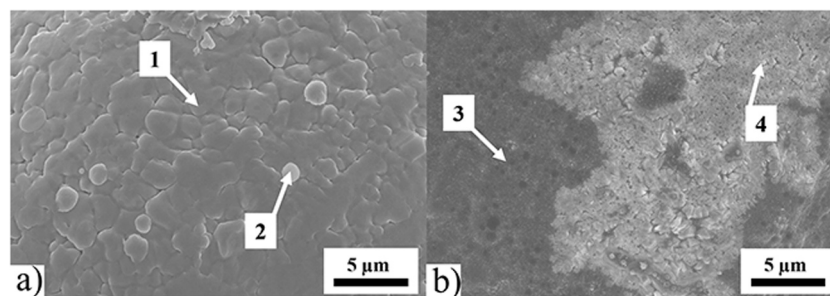

Fig. 4. High-magnification SEM micrographs of the surface of Alloy 718 (a) virgin powder particle and (b) spatter particle generated under 1000 ppm residual oxygen in L-PBF atmosphere. Marked locations were analyzed by EDS, and results are reported in Table 3.

Table 3

EDS analysis from the locations highlighted in Fig. 4 for Alloy 718 virgin powder particles and a spatter produced during L-PBF with 1000 ppm of residual oxygen in the L-PBF atmosphere.

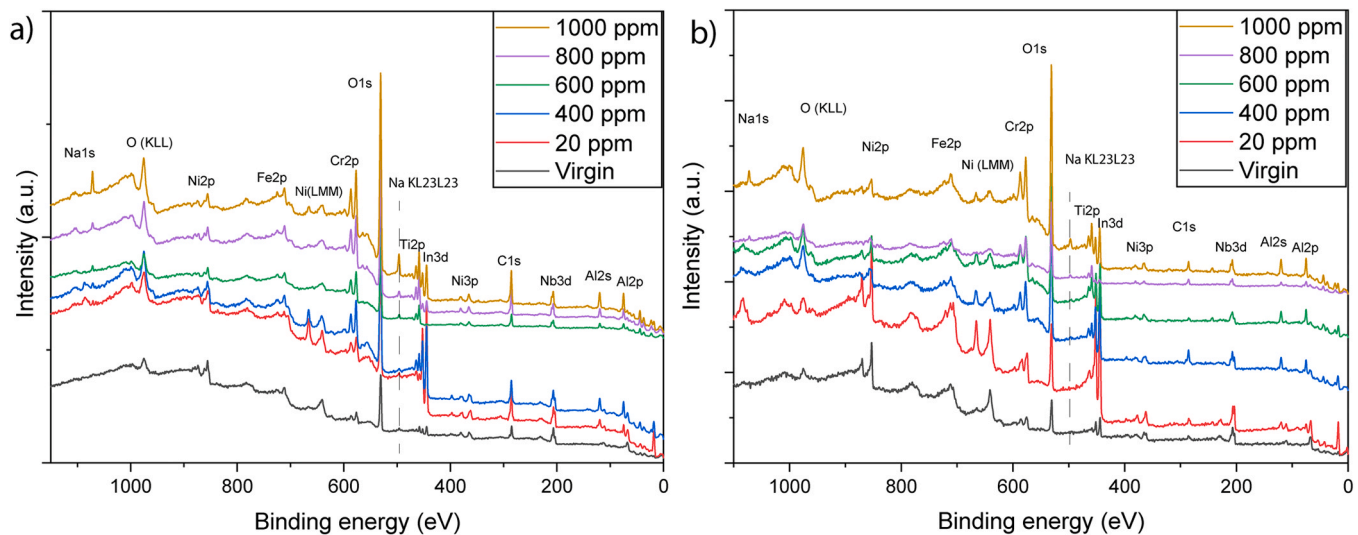| Location	Element	Ni	Cr	Fe	Nb	Mo	Ti	Al	O
Spectrum 1	wt%	52.3	19.4	18.7	3.8	3.4	0.9	0.9	0.6
Virgin	at%	50.5	21.2	18.9	2.3	2.0	1.1	1.8	2.2
Spectrum 2	wt%	50.5	21.2	18.9	2.3	2.0	1.1	1.8	2.2
Virgin	at%	50.9	20.1	18.4	3.4	2.0	1.2	1.1	2.9
Spectrum 3	wt%	48.8	18.0	17.6	3.2	3.0	0.8	3.6	5.0
Spatter 1000 ppm O_2	at%	41.1	17.1	15.5	1.7	1.6	0.9	6.6	15.5
Spectrum 4	wt%	45.5	15.6	13.8	7.7	2.7	1.3	5.9	7.5
Spatter 1000 ppm O_2	at%	36.1	14.0	11.5	3.9	1.3	1.3	10.0	21.9

Fig. 5. Comparison of survey scans between samples taken at different oxygen contents, at (a) as-received surface and (b) at 4 nm etch depth after etching by Ar^+ ions.

in relation to the aluminum content with the Al2s peak of aluminum at ~ 120.1 eV. An increase in intensity was observed from the surface of the virgin powder to that corresponding to the samples processed at 1000 ppm residual oxygen. For the virgin powder, the Al2s peak was negligible due to the minute concentration of Al in the alloy and hence its absence on the powder surface [1], characterized only by a thin layer of oxide corresponding to the matrix composition. However, the Al2s peak appeared in all the spatters from the gas inlet, including those collected after the build job performed with 20 ppm O_2 in the L-PBF atmosphere. This suggests that Al diffusion from the core of the particle toward its surface is active for the spatter particles, confirming an increase in their temperature, enabling diffusion of substitutional elements. This diffusion and oxidation were probably further enhanced via the locally elevated oxygen content by pre-existing oxides on the feedstock powder. Moreover, the relative intensity of the Cr2p peak also increased with the oxygen partial pressure, indicating the pronounced oxidation of Cr alongside Al. This is consistent with the powder surface morphology observations and EDS analysis (Figs. 3 and 4), indicating the formation of particulates or patches on the surfaces of the particles enriched with Al and Cr.

The XPS spectra of the virgin and spatter powders after etching to 4 nm by Ar^+ ions enable analysis of the surface after removal of absorbed species and base oxide layer in the virgin powder, as shown later (Fig. 5b). The same chemical elements were detected on the etched surface as on the as-received surface. The C1s peak was significantly reduced to an extremely low intensity, indicating its origin from absorbed carbon species, typically observed on metal surfaces in the as-received state.

A comparative depth profile analysis was conducted to investigate the variation in type and amount of oxides with etch depth and is displayed in Fig. 6. The Al2s, Cr2p$_{3/2}$, Ni2p$_{3/2}$, and O1s spectra were compared for the samples collected after processing with an atmosphere containing 20 ppm (Fig. 6a), 400 ppm (Fig. 6b), 600 ppm (Fig. 6c), 800 ppm (Fig. 6d), and 1000 ppm (Fig. 6e) residual oxygen.

Indium was used as a template for powder mounting and has an extremely stable and well-distinguished signal along the etch depth, with a stable and well-known peak position. Thus, it was used as an internal standard with the In3d$_{3/2}$ peak at 451.4 eV. Based on the Al2s spectra, the peak position indicated the presence of Al in the cation state as Al^{3+}, with the peak position at ~ 120.09 eV indicating Al-based oxide. The intensity of the Al2s^{3+} peak increased with the residual oxygen in the atmosphere, indicating an increase in the amount of Al-based oxides. The samples obtained with 20 and 400 ppm O_2 showed strong Al2s^{3+} peaks at the surface, which persisted to 20 and 50 nm etch depths, respectively. This highlighted the surface enrichment and oxidation of Al even at low residual oxygen levels. Moreover, the increase in the oxygen partial pressure was associated with the increasing peak intensity and its presence at larger etch depths (below 50 nm), indicating a greater thickness of the oxide phases rich in Al.

The comparison of the Cr2p spectra also showed an increase in the Cr2p$_{3/2}^{3+}$ peak intensity at 577.11 eV compared to the peak of metallic chromium Cr2p$_{3/2}^{met}$ at 574.36 eV near the surface among all samples processed at a high partial pressure of oxygen. This increase persisted at larger etch depths for higher oxygen partial pressure, indicating increased Cr-rich oxide thickness.

The Ni2p spectra are also compared in Fig. 6 to understand the nature of the Cr- and Al-based oxides on the particle surfaces. The presence of Ni oxide on the powder surface was confirmed by analyzing the
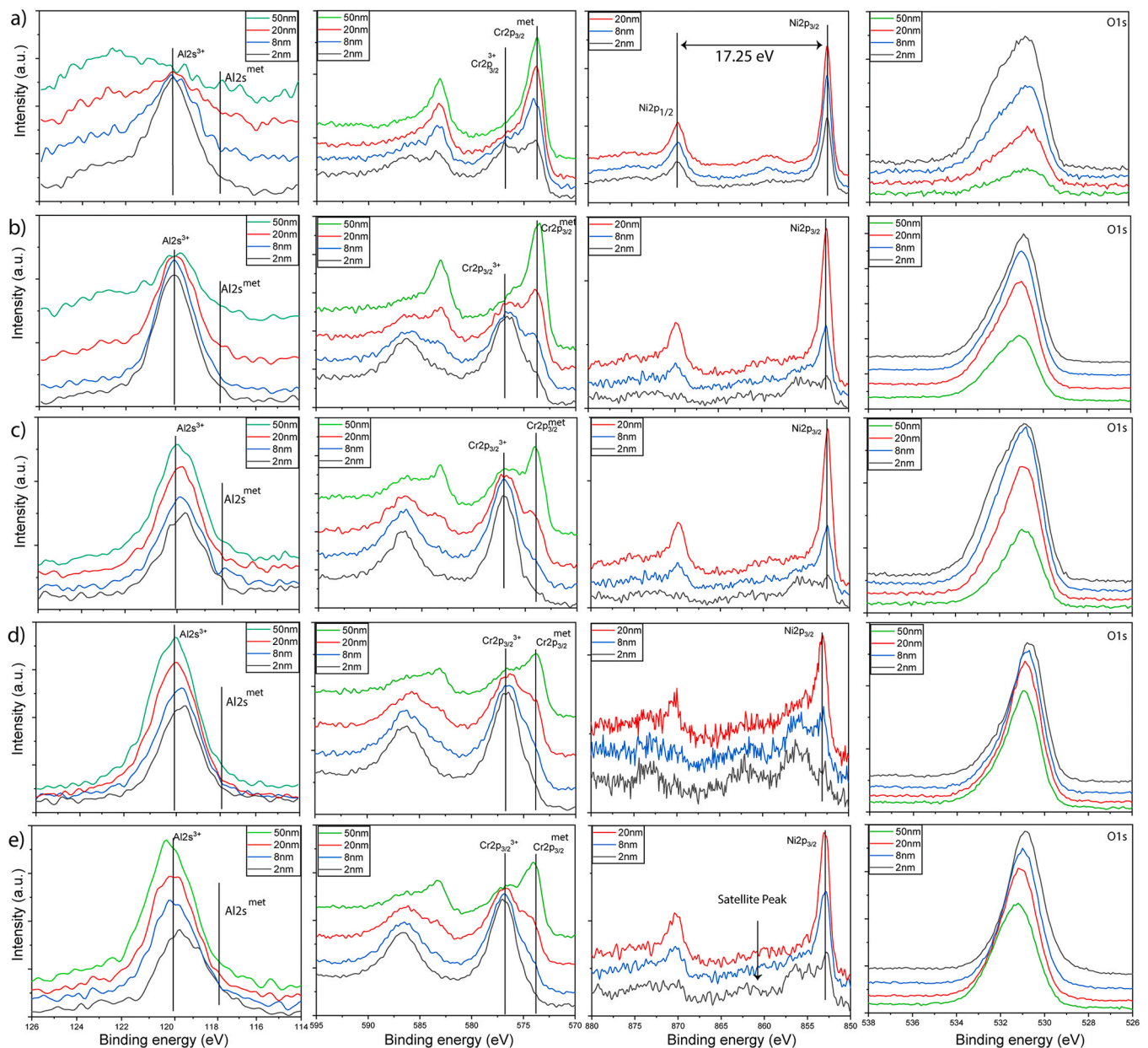
Fig. 6. Comparison of Cr, Al, Ni, and O spectra for the powder samples collected on the gas inlet under residual oxygen levels of (a) 20 ppm, (b) 400 ppm, (c) 600 ppm, (d) 800 ppm, and (e) 1000 ppm.

distance between $Ni2p_{3/2}$ and $Ni2p_{1/2}$ peaks, which should be ~ 17.27 eV for metal and ~ 17.49 eV for oxide [21,22]. Moreover, a satellite peak of $Ni2p_{3/2}$ at ~ 861.8 eV was an additional indication of oxide presence. Ni in its oxide state was observed only to 2 nm, and only metallic Ni was registered at an etch depth of 8 nm for the 20 ppm O_2 spatter. This suggests that the powder surface was covered with a thin Ni-rich oxide layer with a thickness of approximately 2 nm for the spatter processed at a residual oxygen content of 20 ppm, which is close to the surface oxide thickness of the virgin powder. An increased oxygen content in the process atmosphere resulted in a slight increase in the Ni oxide thickness, traces of which were observed to 8 nm with higher residual oxygen contents. Since only trace amounts of Ni oxide were present at depths below 2 nm, its presence was disregarded during further analysis of the oxide composition.

The less pronounced drop in intensity of the oxygen peak for particles collected under higher residual oxygen also confirms the coarsening of oxide species. Additionally, a peak shift toward higher binding

energies with increasing etch depth was noted, which was more significant for the samples processed under 800 and 1000 ppm of residual O_2. The shift represents the higher thickness of Al-based oxide particulates compared with Cr-based oxide particulates and patches. This shift is consistent with the increased intensity of the Al2s peak at higher etch depths.

In a complex alloy such as Alloy 718, peak fitting can provide an insight into the nature and amount of oxides present. Peak fitting of $Cr2p_{3/2}$, O1s, $Ti2p_{3/2}$, and Al1s was conducted, and the results for samples processed at 20 and 1000 ppm of residual oxygen are shown in Fig. 7. Fitting is presented for the spectra measured at 2 nm etch depth after slight Ar-etching that assures removal of the surface absorbed species. The metallic ($Cr2p_{3/2}^{met}$) and oxide ($Cr2p_{3/2}^{3+}$) peaks are positioned at 574.36 and 577.11 eV, respectively. According to the internally measured standard, $Cr2p_{3/2}^{3+}$ measured using Cr_2O_3 should be positioned at 576.60 eV. The current shift represents the mixed nature of Cr-based oxide due to the complex composition of the alloy. In
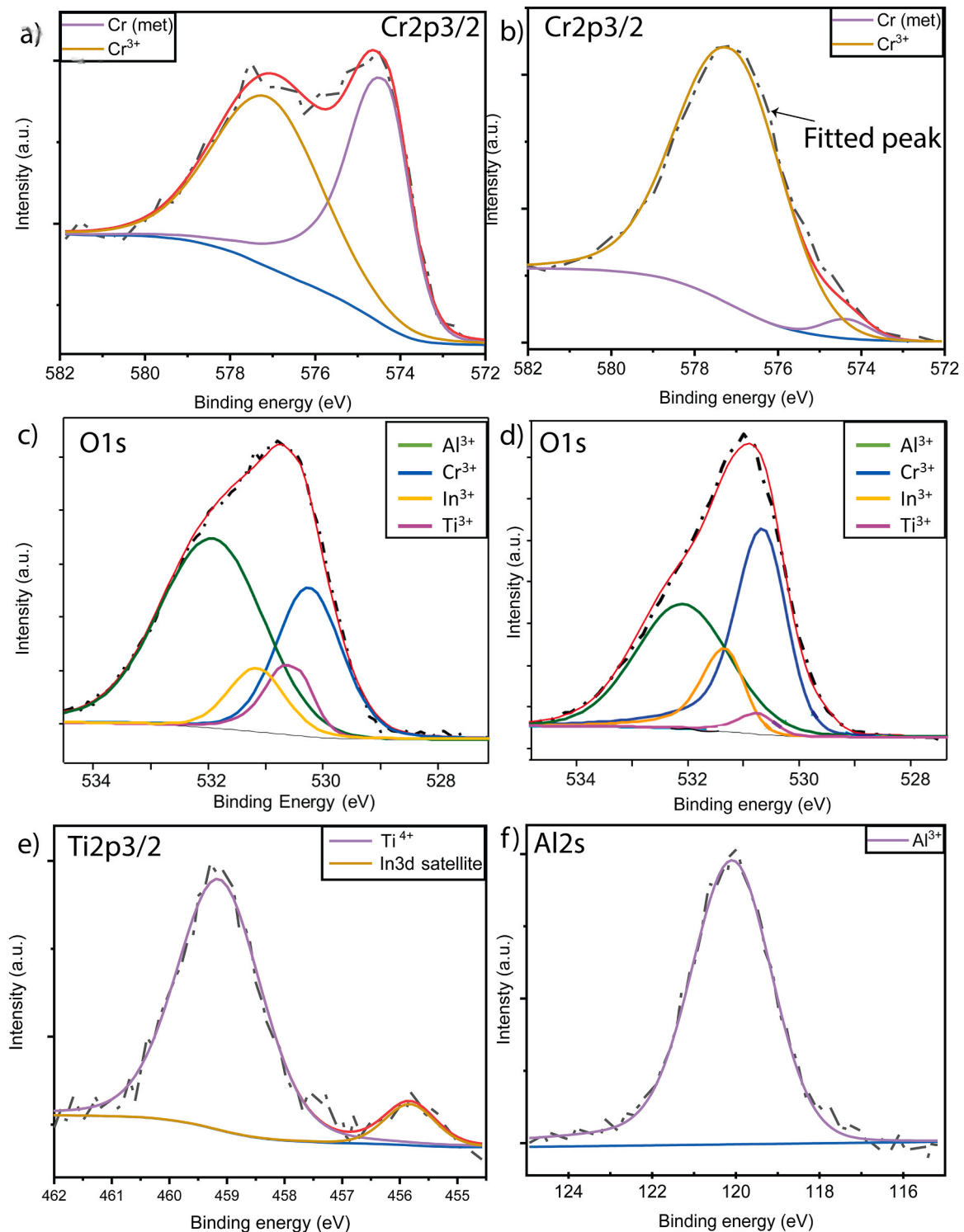
Fig. 7. XPS peak fitting of $Cr2p_{3/2}$ spectra obtained from samples at (a) 20 ppm and (b) 1000 ppm, O1s spectra obtained from samples at (c) 20 ppm and (d) 1000 ppm, (e) $Ti2p_{3/2}$, and (f) Al1s spectra obtained from sample at 1000 ppm at 2 nm etch depth.

the specimen processed at 20 ppm of oxygen, the fraction of $Cr2p_{3/2}^{met}$ was approximately 54.63% of the total peak area (Fig. 7a), indicating a low thickness of the metal oxide covering the powder particles, as well as a low fraction of Cr oxide on the metal surface. The same fitting of the $Cr2p_{3/2}^{met}$ in the sample processed at 1000 ppm (Fig. 7b) indicates the presence of chromium predominantly in the oxide state with only traces of metal with an area below 5%. This highlights a substantial thickening of the Cr-based oxide with an increased residual oxygen content during

L-PBF processing. This trend was also observed for the samples processed at intermediate oxygen contents in the build chamber.

Aluminum was observed only in the oxide state in all cases with the peak position at 120.09 eV. No metallic peak (118 eV) was observed even at higher etch depths; see Figs. 6 and 7f. The same applies to titanium, where only the peak position at $\sim$ 459.10 eV was registered, corresponding to Ti^{4+} (rutile). A small peak at lower binding energy at approximately 455.7 eV in the Ti spectra in Fig. 7e corresponds to the
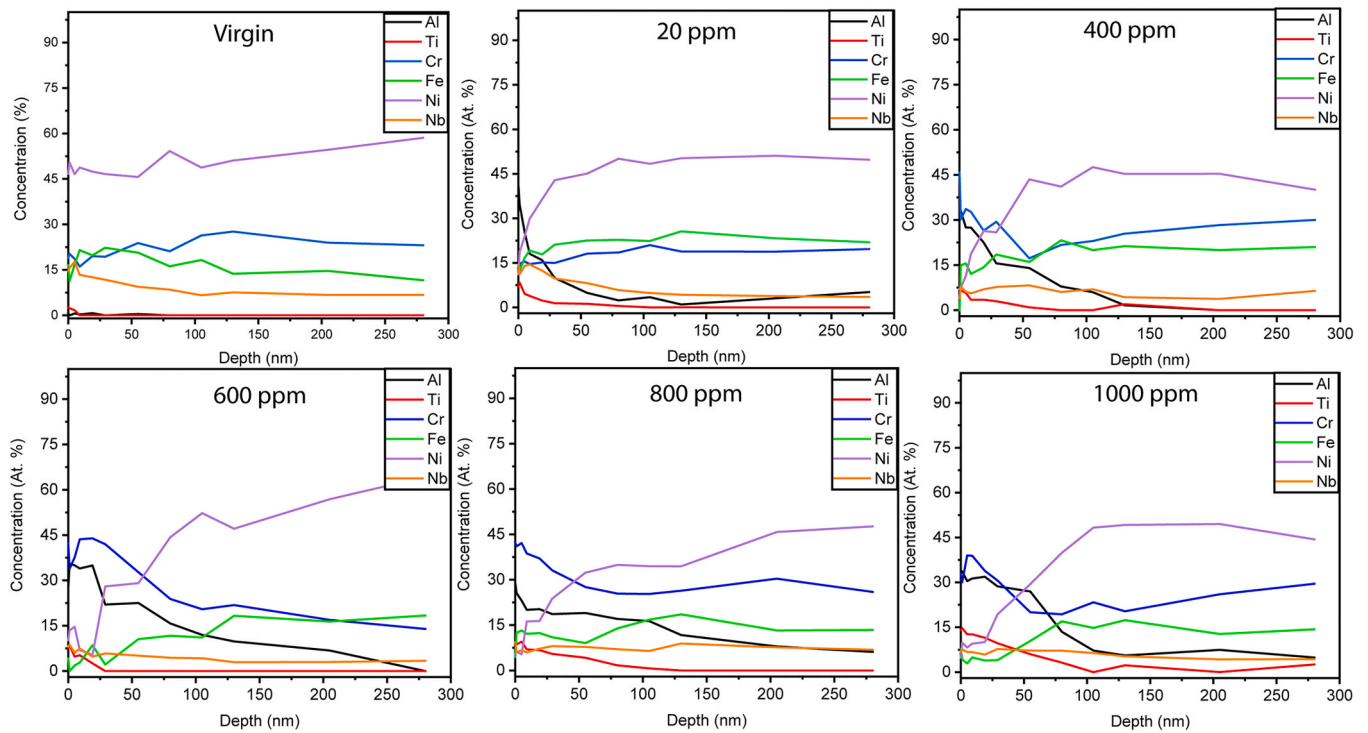
Fig. 8. Normalized chemical composition of metallic elements Al, Ti, Cr, Fe, Ni, and Nb at the surface of the virgin powder and spatters processed at different residual oxygen contents in the process atmosphere.

In3d satellite peak.

The fitting of the O1s spectra provides useful information concerning the relative fractions of different oxide types observed on the powder surface. Due to the low fraction of Ni in the oxide state with the oxygen peak at approximately 529.66 eV, which was below 3% in both cases, this was ignored during fitting. Fig. 7(c and d) represents the relative

fraction of oxide in Al2O3 with O1s at $\sim$ 532.14 eV, Cr2O3 at 530.66 eV, and TiO2 at $\sim$ 530.75 eV. For the fitted O1s spectra, In^{3+} at 531.34 eV originated from the thin oxide/hydroxide layer on the indium plate used as a template for powder sample preparation. Interestingly, the Ti^{4+} peak at 530.75 eV decreased from $\sim$ 10% in area to 4.5% with an increase in the residual oxygen content from 20 to 1000 ppm.
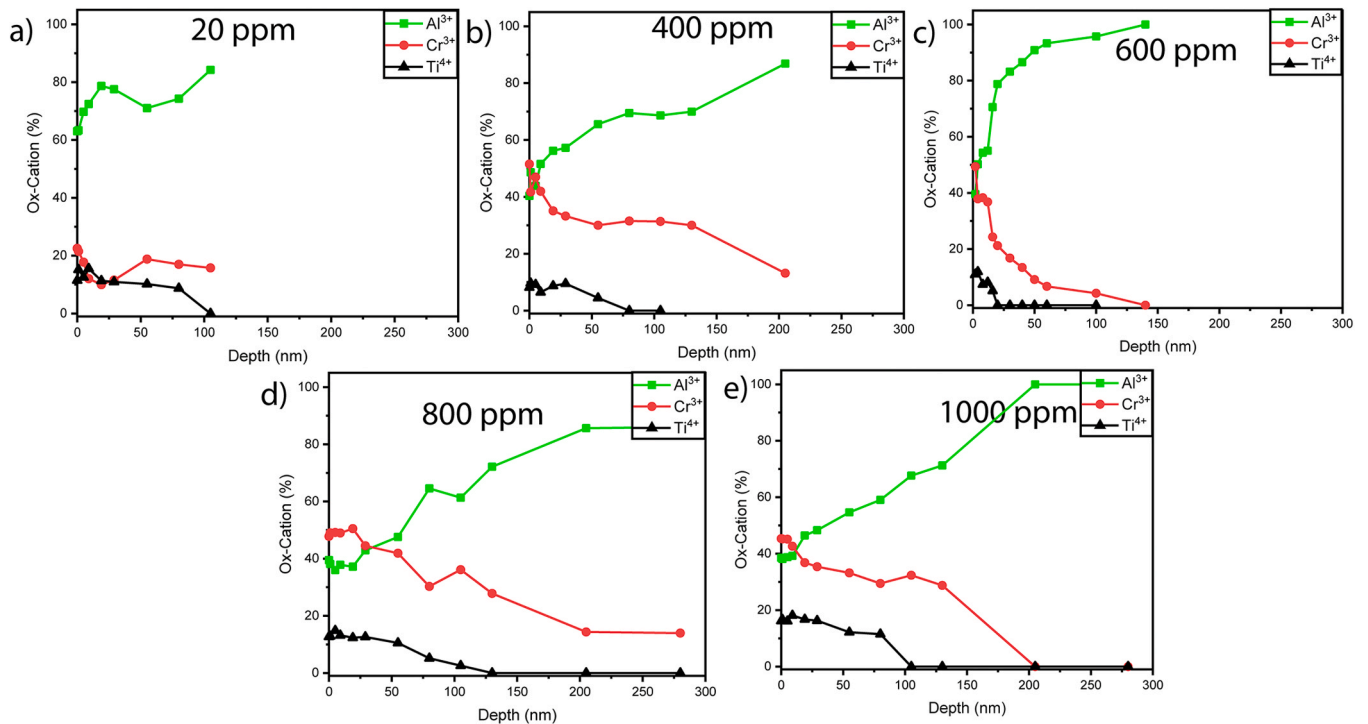

Fig. 9. Comparison of normalized Al, Cr, and Ti cation concentrations for (a) 20 ppm, (b) 400 ppm, (c) 600 ppm, (d) 800 ppm, and (e) 1000 ppm residual oxygen in the process atmosphere.
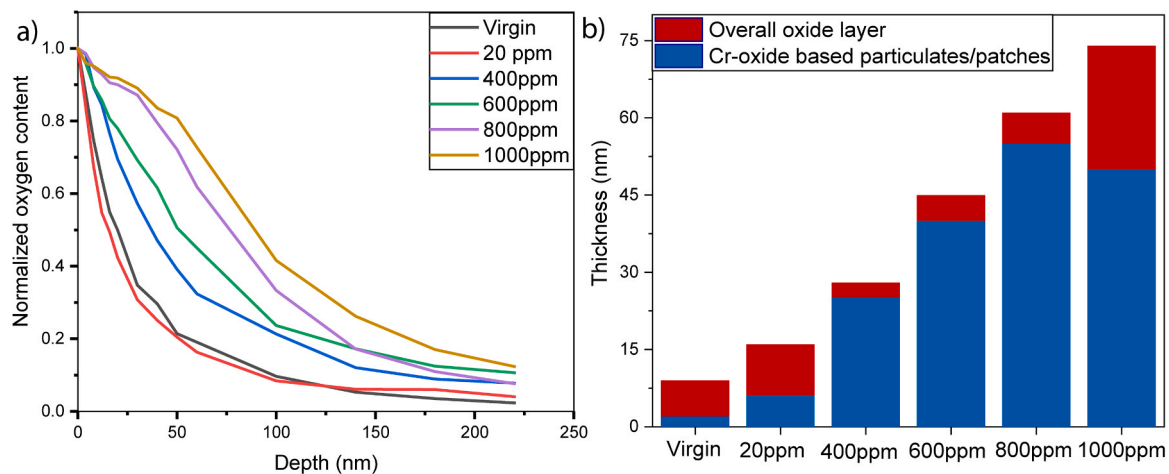
Fig. 10. (a) A comparison of the normalized oxygen content calculated based on the XPS depth profile and (b) calculated Cr-based oxide particulate/patch thickness of all samples.

Considering Al^{3+} at 532.14 eV and Cr^{3+} at 530.66 eV, the amount of Al^{3+} oxide was approximately three times larger than the amount of Cr^{3+} oxide in the 20 ppm sample.

However, in the 1000 ppm sample, the relative amount of Cr^{3+} oxide was comparable to that of Al^{3+} oxide with approximately 5% of the Ti-based oxide, as mentioned above. This confirms that the oxide layer at a lower residual oxygen level was dominated mainly by Al-based oxides due to the high affinity of Al for oxygen compared with Cr as well as its higher diffusivity. However, an increase in the oxygen content in the process atmosphere led to an increase in the fraction of the Cr-based oxide on the spatter surface.

Normalized Al, Cr, Fe, Nb, Ni, and Ti concentrations were calculated based on narrow scans of the binding energies of these elements, where the surface composition in relation to the alloy content was observed (Fig. 8). This also enables further understanding of the enrichment and depletion of certain elements and the surface composition. The virgin powder sample shows a steady composition throughout the depth profile with slight Ti and Cr enrichment on the top surface. The concentration profiles for the sample processed at an oxygen level of 20 ppm confirm Al and Ti enrichment at the surface, where the Al content was enriched by up to 50 times compared to the bulk content of aluminum in the alloy. When comparing the 20 ppm O_2 sample to the 400 ppm one, a significant increase in Al enrichment at the top surface, even at a larger depth of 100 nm, was observed. The concentration near the surface was comparable to the Cr content, which was substantial considering the bulk Al content, which was $\sim$ 36 times lower than the Cr content. Further increasing the oxygen content in the processing atmosphere increased the Al enrichment. The normalized content of Al was higher than that of Cr and Ni near the surface with residual oxygen of 600 ppm. Cr enrichment was also observed starting from higher oxygen contents, reaching a factor of two compared with the bulk content of chromium at higher residual oxygen levels in the processing gas. Both Ni and Fe showed consistently increased depletion from the surface with an increase in residual oxygen. Niobium was present in nominal amounts in all the samples and showed no significant variation.

A normalized calculation of Al^{3+}, Cr^{3+}, and Ti^{4+} cations was performed to differentiate between the chemical composition and cation concentration (Fig. 9). Due to the low fraction of Ni in the surface oxide and presence of Nb and Fe in mainly the metallic state, these were ignored when calculating the cation concentrations to focus on the main oxide formers, Al, Cr, and Ti. In all the presented samples, Ti^{4+} cations existed in relatively smaller fractions than Al^{3+} and Cr^{3+} cations. At higher oxygen levels in the build chamber, Ti^{4+} cations were present at larger etch depths, highlighting the coarsening of oxides on spatter particles. Al^{3+} enrichment was more dominant than Cr^{3+} throughout the

depth profile. At 20 ppm, the amount of Al^{3+} cations was three to four times larger than the amount of Cr^{3+} cations at the surface. The concentration profiles of Al^{3+} and Cr^{3+} indicate relative enrichment of Al-based oxides with increased etch depths, especially with increasing oxygen content in the processing atmosphere, suggesting the formation of coarse Al-rich particulate oxide phases on the surfaces of the spatter particles. These results were also confirmed by oxide traces extending from approximately 50 to above 250 nm with increased oxygen content in the process atmosphere from below 20 to above 1000 ppm. It is noteworthy that traces of the oxides were observed at larger etch depths than the actual thickness of the surface oxide due to a shadowing effect that is a characteristic feature of XPS analysis of irregular powder samples [20].

Finally, the normalized oxygen content along the etch depth enabled evaluation of the oxide layer thickness [19,20] and effective comparison of the extent of surface oxidation of the powders studied. A comparative plot of the normalized oxygen content of all the examined samples is given in Fig. 10a. The increase in oxygen partial pressure led to a substantial increase in the normalized oxygen content in the respective samples at larger etch depths. The findings are consistent with the cation concentrations as well as the oxygen depth profiles. In the oxygen depth profile shown in Fig. 6, a strong peak was observed at an etch depth of 50 nm in the 1000 ppm residual O_2 sample in contrast with the sample processed at 20 ppm O_2. The thickness of Cr-rich oxide patches/-particulates were calculated using the relative intensity of the Cr^{3+} peak (Fig. 10b). The initial thickness of approximately 2 nm on the virgin powder corresponds to the thickness of the oxide layer covering the powder particles. A drastic increase in thickness was observed when the residual oxygen was increased to 400 and 600 ppm, for which it reached 28 and 40 nm, respectively. Finally, the Cr-based oxide particulate or patch thickness peaked for 800 ppm residual oxygen in the process chamber and was estimated as $\sim$ 56 nm. This tendency for the Cr-based oxide thickness to increase further confirms the relationship between the residual oxygen and spatter oxidation. The plot in Fig. 10b also provides information about the overall oxide thickness determined from the oxygen peaks. The analysis shows a consistent increase in oxide layer thickness with residual oxygen content, consistent with the other findings.

Comparing the normalized oxygen content and oxide particulate/patch thickness highlights an extremely important conclusion – as the oxygen content in the powder increased with a higher residual oxygen partial pressure during L-PBF processing, the additional oxygen was not consumed by the formation or growth of Ni-based oxide but instead led to the formation of Al- and Cr-based oxides on the spatter surface of the Alloy 718 powder.
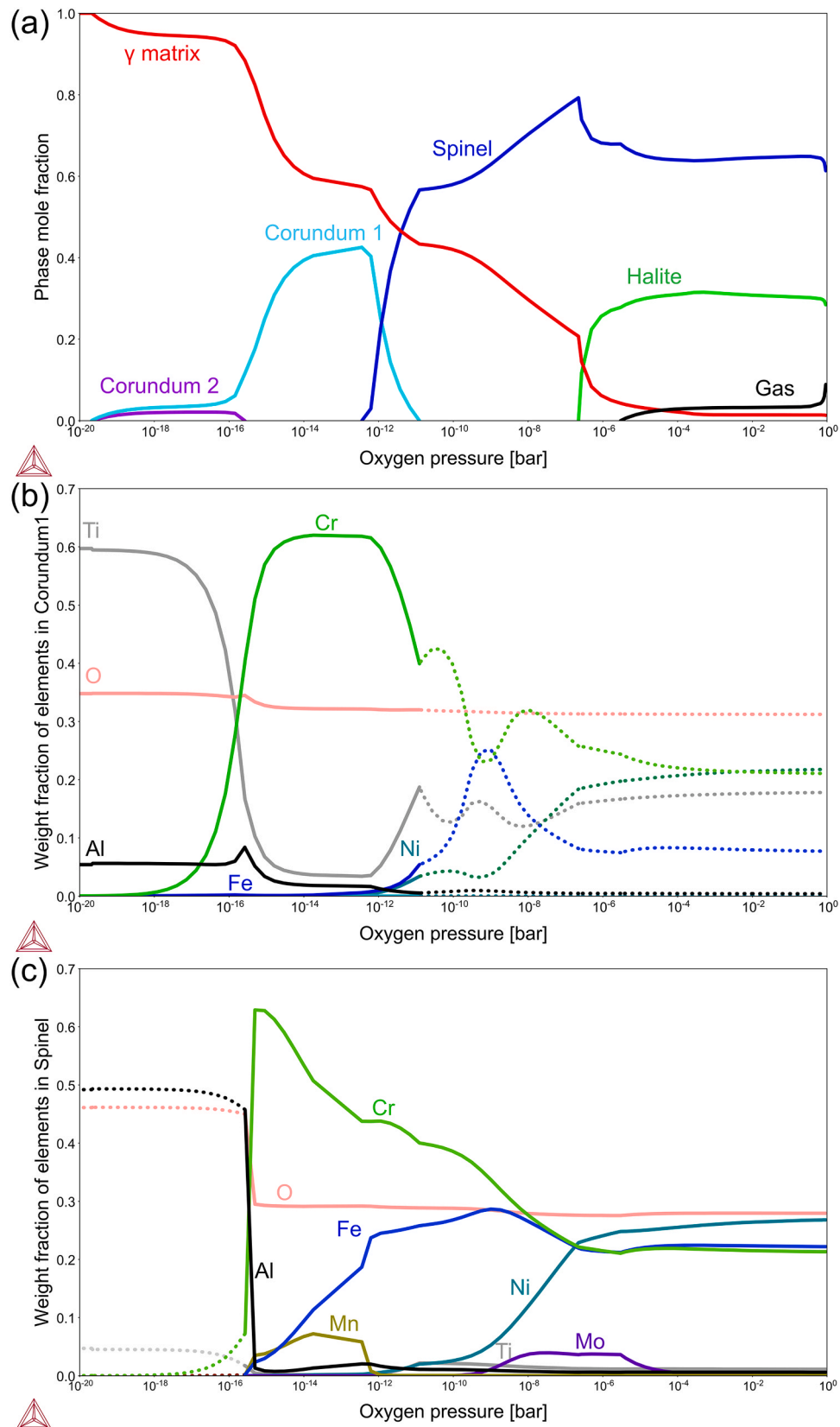
Fig. 11. Thermodynamic calculations using Thermo-Calc 2021: (a) equilibrium phase fraction at 1300 °C with varying oxygen partial pressure, (b) composition of corundum 1 phase, and (c) composition of spinel phase. The dashed lines correspond to the elemental compositions in the metastable phase.
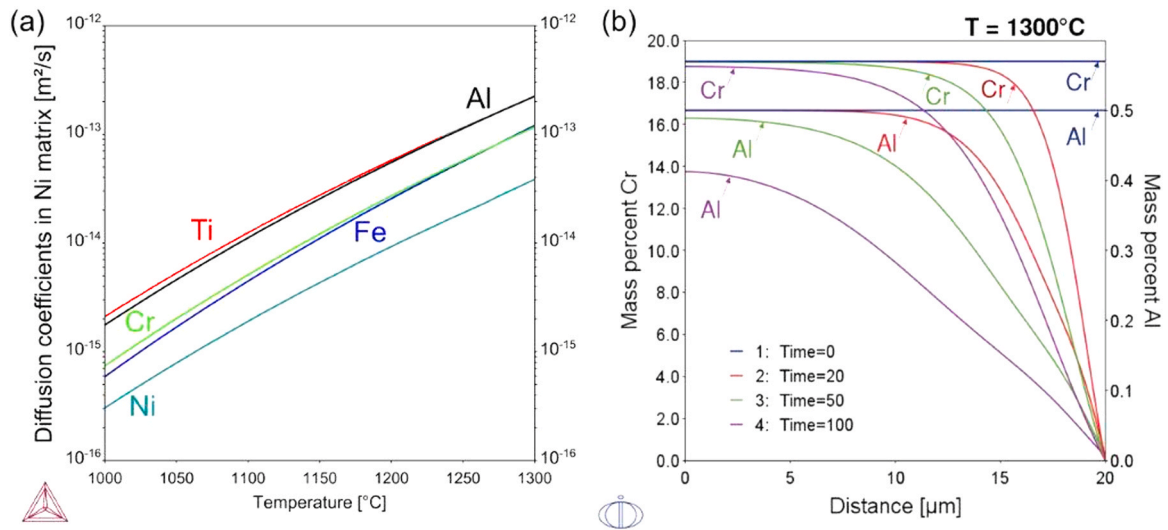
Fig. 12. (a) Diffusion coefficients of Al, Ti, Cr, Fe, and Ni in the Ni austenitic FCC matrix. (b) Concentration profiles of Al and Cr in Ni in a 20 μm radius particle at 1300 °C, considering the activity of Al and Cr based on the FCC/corundum and FCC/spinel equilibria, respectively.

Thermodynamic calculations were performed using Thermo-Calc software (2021a, TCOX10 database) to further elaborate on the findings from the experimental analysis of the spatter particles. Our previous work highlighted that entrained spatters represented the largest fraction of the generated spatters [8]. Observing the spatter cross-section revealed that entrained spatters retained their microstructure inherited from gas atomization despite surface oxidation. Conversely, direct melt pool ejections were expelled in a molten state, solidifying during flight, when falling on the powder bed, or colliding with other particles. They underwent faster cooling (10^8 K/s compared to 10^6 K/s), resulting in finer primary dendrite arm spacing than for entrained particles [8]. Therefore, the Thermo-Calc calculation was conducted considering the alloy at a high temperature, 1300 °C, but still in the solid state, mimicking the state of a heated entrained particle, most representative of the generated spatters.

Fig. 11a depicts the calculated equilibrium phase composition for Alloy 718 with varying oxygen activity at 1300 °C. At a minimal oxygen pressure (below 10^{-16} bar), a corundum phase containing Al- and Ti-

based oxides was stable, as shown in Fig. 11b (see *Corundum 1*). Due to the small concentration of Al and Ti in the alloy and a higher concentration of Cr, an increase in the oxygen partial pressure was accompanied by a substantial increase in the Cr content in the corundum phase with a persisting amount of Al. Additionally, the spinel phase was stable at higher oxygen pressure, dominated by Al to approximately 10^{-15} bar of oxygen (Fig. 11c), with further enrichment by Cr, Mn, Fe, and Ni with an increased partial pressure of oxygen. Together with the XPS results, this indicates the formation of Al-rich oxide at low partial pressures (virgin and powder samples processed at 20 ppm), with subsequent enrichment with Cr with increasing oxygen potential. However, although thermodynamic calculations demonstrate the thermodynamic stability of oxides at different partial pressures of oxygen, considering the high cooling rates experienced by spatters [8], it is important to also consider the kinetic aspects of oxide formation during such a short exposure.

Using Thermo-Calc 2021a and the TCNI10 and MOBNI5 databases, the diffusion coefficients of the main oxide-forming elements present in
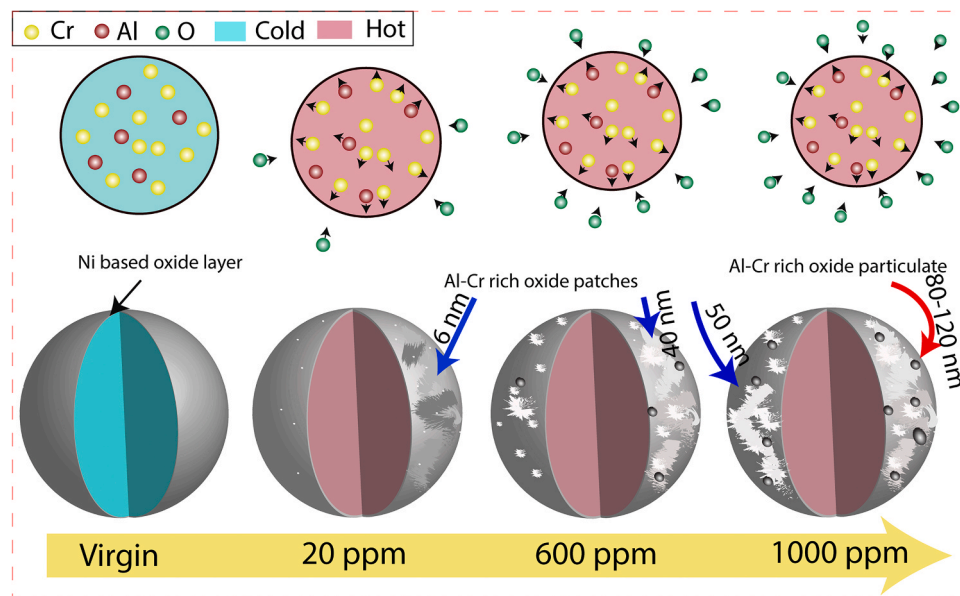

Fig. 13. Schematic model highlighting the relationship between residual oxygen partial pressure during L-PBF and extent of oxidation of Alloy 718 spatter powder particles.

Alloy 718 at high temperatures were plotted using the diffusion module DICTRA of Thermo-Calc (Fig. 12a). Al and Ti evidently have considerably higher diffusivity than Cr and Fe. In the oxidation of Alloy 718 spatter particles, Al and Cr diffusion was simulated in a 20 μm radius particle. Herein, the surface conditions were defined considering the Al and Cr activities derived from the equilibrium calculation (Fig. 11), and more particularly the FCC/corundum equilibrium for Al and the FCC/spinel equilibrium for Cr. Fig. 12b displays the concentration profiles for Al and Cr at 1300 °C for different times: 0, 20, 50, and 100 s. Similar diffusion profiles, indicating more rapid diffusion of Al to the surface where oxidation occurs, were obtained at lower temperatures based on the difference in diffusivities between Al and Cr, see Fig. 12a.

The findings of this study are illustrated with a schematic model in Fig. 13. As-received powder particles had a thin layer of Ni-based oxide, whose composition approximately represented the alloy composition. As the entrained particles collected on the gas inlet were partially exposed to the heat, some surface regions were more oxidized than others. For spatters produced with the lowest residual oxygen level (20 ppm), low oxygen potential resulted in the formation of extremely thin – approximately 6 nm in thickness – mixed Cr-Al-oxide. However, an increase to 600 ppm residual oxygen in the L-PBF process chamber resulted in changes in the amount and morphology of the oxides. The amount and thickness of oxide patches and particulates consistently increased with the residual oxygen level up to the standard level of 1000 ppm or 0.1%.

4. Conclusions

The conducted investigations highlight the major role of the process atmosphere's purity in the spatter oxidation and hence powder degradation during L-PBF processing of Alloy 718. The results indicate that reducing the residual oxygen level in the process chamber and thus in the vicinity of the powder bed slows the oxidation kinetics of Alloy 718 spatter particles. The following conclusions are drawn based on the obtained results:

- The spatter particles deposited on the gas inlet during L-PBF mainly comprised large-diameter entrained particles and, to a smaller extent, projections from the melt pool, with clear evidence of oxidation.
- The study of the collected particles using HR-SEM combined with EDS highlighted an increasing coverage of the powder surface by oxide features rich in Al and Cr and traces of Ti with increasing partial pressure of oxygen in the L-PBF process atmosphere from 20 ppm to the standard level of 1000 ppm O_2.
- Reducing the oxygen concentration in the L-PBF process atmosphere below the typical 1000 ppm threshold mitigated this critical spatter oxidation, reflected in the reduced oxygen and nitrogen contents in the sampled spatter powder. The spatter produced under 20 ppm O_2 showed contents of 206 ppm O and 107 ppm N, compared with 608 ppm O and 117 ppm N for that generated under 1000 ppm O_2 and 150 ppm of O and 90 ppm of N in the virgin powder.
- The chemical composition and thickness of surface oxides, investigated through XPS, showed that Al- and Cr-rich oxides were predominantly formed on the spatter surfaces.
- The thickness of the Cr-rich oxide patches, determined by XPS, showed a drastic increase for lower atmospheric purities, reaching a thickness above 50 nm for a high partial pressure of oxygen in the system.
- A combined XPS and thermodynamic analysis highlighted a fundamental transition from Al-dominated oxide at lower residual oxygen levels to Al- and Cr-dominated oxide layers at higher oxygen levels.

Increasing the purity of the process atmosphere – or decreasing the residual oxygen content –efficiently mitigated the spatter oxidation and hence powder degradation during L-PBF processing of Alloy 718. This

study suggests that by operating L-PBF for Alloy 718 at ∼ 20 ppm residual oxygen content, the oxide layer thickness formed on spatter particles can be reduced, and their oxygen content limited to an increase of ∼ 30% compared to the virgin powder. Based on the detrimental role of spatters in powder degradation, this reduced oxidation will increase the reusability of powder, compensating for the slight increase in cost incurred by using high-purity gas.

CRediT authorship contribution statement

Ahmad Raza: Conceptualization, Methodology, Investigation, Formal analysis, Visualization, Writing – original draft. **Camille Pauzon:** Conceptualization, Investigation, Formal analysis, Writing – original draft. **Eduard Hryha:** Conceptualization, Methodology, Funding acquisition, Project administration, Supervision, Writing – review & editing. **Andreas Markström:** Software, Formal analysis. **Pierre Forêt:** Resources, Supervision, Writing – review & editing.

Declaration of Competing Interest

The authors declare that they have no known competing financial interests or personal relationships that could have appeared to influence the work reported in this paper.

Acknowledgments

References

[1] H. Gruber, M. Henriksson, E. Hryha, L. Nyborg, Effect of powder recycling in electron beam melting on the surface chemistry of alloy 718 powder, Metall. Mater. Trans. A Phys. Metall. Mater. Sci. 50 (2019) 4410–4422, https://doi.org/10.1007/s11661-019-05333-7.
[2] M.C. Chaturvedi, Y.F. Han, Strengthening mechanisms in Inconel 718 superalloy, Met. Sci. 17 (1983) 1–5, https://doi.org/10.1179/030634583790421032.
[3] E. Hryha, R. Shvab, H. Gruber, A. Leicht, L. Nyborg, Surface oxide state on metal powder and its changes during additive manufacturing: an overview, Proc. Eur. PM 2017 Int. Powder Metall. Congr. Exhib. (2018).
[4] A.N.D. Gasper, D. Hickman, I. Ashcroft, S. Sharma, X. Wang, B. Szost, D. Johns, A. T. Clare, Oxide and spatter powder formation during laser powder bed fusion of Hastelloy X, Powder Technol. 354 (2019) 333–337, https://doi.org/10.1016/j.powtec.2019.06.004.
[5] E. Santecchia, S. Spigarelli, M. Cabibbo, Material reuse in laser powder bed fusion: side effects of the laser—metal powder interaction, Metals 10 (2020) 1–21, https://doi.org/10.3390/met10030341.
[6] C. Pauzon, E. Hryha, P. Forêt, L. Nyborg, Effect of argon and nitrogen atmospheres on the properties of stainless steel 316L parts produced by laser-powder bed fusion, Mater. Des. 179 (2019), 107873, https://doi.org/10.1016/j.matdes.2019.107873.
[7] A. Raza, T. Fiegl, I. Hanif, A. Markström, M. Franke, C. Körner, E. Hryha, Degradation of AlSi10Mg powder during laser based powder bed fusion processing, Mater. Des. 198 (2021), 109358, https://doi.org/10.1016/j.matdes.2020.109358.
[8] C. Pauzon, A. Raza, E. Hryha, P. Forêt, Oxygen balance during laser powder bed fusion of Alloy 718, Mater. Des. 201 (2021), https://doi.org/10.1016/j.matdes.2021.109511.
[9] H. Gruber, P. Karimi, E. Hryha, L. Nyborg, Effect of powder recycling on the fracture behavior of electron beam melted alloy 718, Powder Metall. Prog. 18 (2018) 40–48, https://doi.org/10.1515/pmp-2018-0005.
[10] C.L.A. Leung, S. Marussi, M. Towrie, R.C. Atwood, P.J. Withers, P.D. Lee, The effect of powder oxidation on defect formation in laser additive manufacturing, Acta Mater. 166 (2019) 294–305, https://doi.org/10.1016/j.actamat.2018.12.027.
[11] L.C. Ardila, F. Garciandia, J.B. González-Díaz, P. Álvarez, A. Echeverria, M. M. Petite, R. Deffley, J. Ochoa, Effect of IN718 recycled powder reuse on properties of parts manufactured by means of Selective Laser Melting, in: Phys. Procedia, Elsevier B.V, 2014, pp. 99–107, https://doi.org/10.1016/j.phpro.2014.08.152.
[12] S. Ly, A.M. Rubenchik, S.A. Khairallah, G. Guss, M.J. Matthews, Metal vapor micro-jet controls material redistribution in laser powder bed fusion additive manufacturing, Sci. Rep. 7 (2017) 1–12, https://doi.org/10.1038/s41598-017-04237-z.
[13] M.J. Matthews, G. Guss, S.A. Khairallah, A.M. Rubenchik, P.J. Depond, W.E. King, Denudation of metal powder layers in laser powder bed fusion processes, Acta Mater. 114 (2016) 33–42, https://doi.org/10.1016/j.actamat.2016.05.017.

[14] A. Bin Anwar, Q.C. Pham, Study of the spatter distribution on the powder bed during selective laser melting, Addit. Manuf. 22 (2018) 86–97, https://doi.org/10.1016/j.addma.2018.04.036.

[15] V. Gunenthiram, P. Peyre, M. Schneider, M. Dal, F. Coste, I. Koutiri, R. Fabbro, Experimental analysis of spatter generation and melt-pool behavior during the powder bed laser beam melting process, J. Mater. Process. Technol. 251 (2018) 376–386, https://doi.org/10.1016/j.jmatprotec.2017.08.012.

[16] C. Pauzon, P. Forêt, E. Hryha, T. Arunprasad, Effect of helium - argon mixtures as laser - powder bed fusion processing atmospheres on the properties of the built Ti-6Al-4V Parts, WorldPM 2018 (2018) 1633–1639.

[17] K. Dietrich, J. Diller, S. Dubiez-le Goff, D. Bauer, P. Forêt, The influence of oxygen on the chemical composition and mechanical properties of Ti-6Al-4V during laser powder bed fusion (L-PBF), Addit. Manuf. 32 (2020), https://doi.org/10.1016/j.addma.2019.100980.

[18] C. Pauzon, K. Dietrich, P. Forêt, S. Dubiez-Le Goff, E. Hryha, G. Witt, Control of residual oxygen of the process atmosphere during laser-powder bed fusion processing of Ti-6Al-4V, Addit. Manuf. (2020), https://doi.org/10.1016/j.addma.2020.101765.

[19] C. Oikonomou, D. Nikas, E. Hryha, L. Nyborg, Evaluation of the thickness and roughness of homogeneous surface layers on spherical and irregular powder particles, Surf. Interface Anal. 46 (2014) 1028–1032, https://doi.org/10.1002/sia.5439.

[20] E. Hryha, C. Gierl, L. Nyborg, H. Danninger, E. Dudrova, Surface composition of the steel powders pre-alloyed with manganese, Appl. Surf. Sci. 256 (2010) 3946–3961, https://doi.org/10.1016/j.apsusc.2010.01.055.

[21] A.N. Mansour, Characterization of NiO by XPS, Surf. Sci. Spectra 3 (1994) 231–238, https://doi.org/10.1116/1.1247751.

[22] J.F. Moulder, W.F. Stickle, P.E. Sobol, K.D. Bomben, Handbook of X-ray photoelectron spectroscopy: a reference book of standard spectra for identification and interpretation of XPS data, Phys. Electron.: Eden Prairie, MN 1995 (2000) 261. ⟨https://www.cnyn.unam.mx/~wencel/XPS/MANXPS.pdf⟩.